A Novel High-Resolution Wide-Swath SAR Imaging Mode Employing Multichannel Slow PRI Variation

Felipe Queiroz de Almeida, Gerhard Krieger
German Aerospace Center (DLR), Microwaves and Radar Institute, felipe.queirozdealmeida@dlr.de
Wessling, Germany

Abstract

High resolution and wide swath imaging are conflicting requirements in the design of spaceborne synthetic aperture radar (SAR) systems. Several studies have shown that this fundamental conflict can be resolved by advanced instrument modes and architectures employing multiple receive channels in elevation and/or azimuth. This paper introduces a new high-resolution wide-swath SAR imaging mode that uses multiple elevation and azimuth beams in combination with a slow variation of the pulse repetition interval (PRI). It is shown that this new mode enables the development of a highly performant SAR system with a rather compact antenna. As an example, the design of an L-band system is presented that is capable of imaging a 400 km wide swath with an azimuth resolution of 5 m in single polarization. A detailed analysis reveals that an excellent performance is achieved by combining a digital feed with 3 azimuth and 30 elevation channels using an unfurlable reflector that spans a diameter of 12 m. If compared to the staggered SAR mode of Tandem-L, which will employ a reflector with a diameter of 15 m, the required antenna aperture is reduced in the new mode by more than 35 %. Moreover, the same architecture enables the operation in a multichannel staggered SAR mode, which allows for the mapping of a 200 km wide swath with an even higher azimuth resolution of less than 2.5 m in a fully polarimetric mode.

1 Introduction

Spaceborne Synthetic Aperture Radar (SAR) systems for remote sensing are subject to a well-known compromise between the best azimuth resolution and the maximum swath width [1]. ScanSAR [2],[3] is a well-established imaging mode in which a wide swath composed of several sub-swaths is imaged by means of alternately illuminating each sub-swath. The available illumination time is shared between a number of bursts covering different regions on the ground, trading off azimuth resolution for wider coverage.

Multichannel architectures combined with *digital beamforming* (DBF) [4],[5],[6],[7] show the capability of overcoming this limitation and simultaneously delivering *high-resolution wide-swath* (HRWS) SAR images. One family of methods derives from the use of multiple channels in elevation [8],[9],[10]. A system capable of simultaneously forming multiple elevation beams (MEB) through DBF can be used to image several sub-swaths at once, extending the SCan-On-Receive (SCORE) [11] concept. A broad transmit beam is used to illuminate all sub-swaths, whereas multiple narrow receive beams follow simultaneously a set of radar echoes arriving from different directions. In comparison to a concept with multiple azimuth channels [12], the use of multiple elevation channels has the potential to lead to a more compact antenna design [9] and simpler signal processing.

An inherent limitation remains in the form of *blind ranges* between the sub-swaths. These are formed due to the impossibility of recording the echoes while transmitting – a characteristic of monostatic systems – and have regularly spaced positions determined by the (constant) PRF. An interesting extension of this system [8],[9] would be a multi-elevation beam ScanSAR with two-bursts, whose pulse repetition intervals (PRI) admit two values chosen as to be complementary in terms of the *blind ranges*, as shown in **Figure 1 (a)**. Notice that this may be regarded as a particularly simple form of PRI variation (analyzed in a broader context in [13]), in which the instantaneous PRI curve is a square-wave.

A different strategy would be to allow the PRI to slowly vary between the two extreme values, as illustrated in **Figure 1 (b)**. A slow and linear PRI variation, repeated cyclically, causes the PRI curve to become a saw-tooth waveform. As a consequence, the transmit (Tx) induced gaps migrate slowly across the swath, inducing gaps in the Doppler spectrum. Their length will, however, be determined by the extent of the transmission events (i.e. duty cycle), instead of the number of sub-swaths. This represents an opportunity to increase the effective observation time in comparison to a conventional ScanSAR mode. The PRI variation has the downside of leading to a non-uniformly sampled azimuth signal. At the cost of a slight oversampling in azimuth, the signal can be regularized by interpolation, which takes a particular simple form due to the relatively small deviations from uniform sampling. Owing to the slow variation, linear interpolation may be applied instead of the more advanced algorithms required to interpolate across the gaps in the fast PRI variation criterion (cf. [13]).

The new imaging mode with slowly varying PRI and multiple elevation beams will be analyzed in Section 2, in which a concept for azimuth DBF is also introduced, taking advantage of the mode's properties. Section 3 provides performance simulation examples, assuming a multichannel system which is, in addition, able to operate in a complementary multichannel staggered SAR [14] mode. Finally, the paper is concluded in Section 4 with a summary and discussion of the introduced concepts and the performance assessment results.

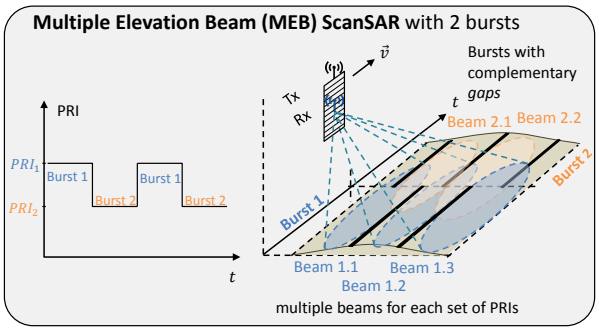

(a)

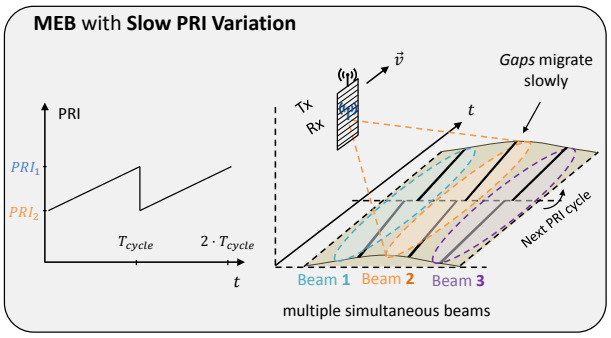

(b)

Figure 1: Schematic representation of imaging modes. (a) Multiple elevation beam (MEB) system with two bursts and two different PRIs. At each burst, sub-swaths separated by *blind ranges* are simultaneously imaged. The two PRIs are chosen such that the blind ranges of one burst are covered by the other, combining into a gapless swath. (b) MEB system with slow pulse-to-pulse PRI variation where Tx-induced gaps migrate continuously.

2 Mode Description

This section describes the aforementioned slowly varying PRI mode mathematically and discusses its properties. Section 2.1 addresses the timing characteristics of the mode and derives a criterion for a first-order design. Section 2.2 discusses the signal's Doppler spectrum, which motivates the azimuth antenna pattern design and DBF concept proposed in Section 2.3.

2.1 Timing Analysis

To analyze the mode in more detail, we start from a constant PRF SAR operated at a sampling interval of PRI between pulses of duration τ_P. The corresponding gaps, whose signal cannot be recorded due to the pulse transmission, correspond to the ranges

$$\frac{c}{2}\cdot k\cdot PRI \le R_{blind}(k) \le \frac{c}{2}\cdot k\cdot PRI + \tau_P, \tag{1}$$

for integer k, which defines the return order. Now, allow the system's PRI to undergo a slow linear variation between PRI_{min} and PRI_{max}, during a period of T_{cycle}. If the swath of interest extends between R_{min} and R_{max}, the orders of interest lie in the interval

$$\left\lfloor \frac{2\cdot R_{min}}{c}\cdot\frac{1}{PRI_{max}} \right\rfloor \le k \le \left\lfloor \frac{2\cdot R_{max}}{c}\cdot\frac{1}{PRI_{min}} \right\rfloor. \tag{2}$$

Ignoring the effect of the travelling pulses and assuming that the PRI variation sequence is long and smooth enough to be treated as continuous, the ranges corresponding to the beginning and end of the blocked return regions are given, for a fixed order k, by

$$\begin{aligned} R_1(t) &= \frac{c}{2}\cdot k\cdot\left(PRI_{max} - \frac{\Delta PRI}{T_{cycle}}\cdot t\right) \\ R_2(t) &= \frac{c}{2}\cdot\left[k\cdot\left(PRI_{max} - \frac{\Delta PRI}{T_{cycle}}\cdot t\right) + \tau_P\right]. \end{aligned} \tag{3}$$

Hence, the azimuth gap length for a given range R_0 can be obtained by setting $R_0 = R_1(t_1) = R_2(t_2)$ and calculating $T_{gap} = t_2 - t_1$, which leads to

$$T_{gap}(k) = \frac{\tau_P}{k}\cdot\frac{T_{cycle}}{PRI_{max} - PRI_{min}}. \tag{4}$$

Albeit long, the PRI variation sequence is discrete. Assuming a sequence with length N_{PRI}, the PRI varies as

$$PRI[n] = PRI_{max} - n\cdot\frac{\Delta PRI}{N_{PRI}-1}, \tag{5}$$

$0 \le n \le N_{PRI} - 1$, and the cycle has a total duration

$$T_{cycle} = \sum_{n=0}^{N_{PRI}-1} PRI[n] = N_{PRI}\cdot\left(PRI_{max} - \frac{\Delta PRI}{2}\right). \tag{6}$$

The delay corresponding to a given number k of travelling pulses (the beginning of the k^{th} transmit/blockage event) starting from pulse i may be defined as

$$d_{i,k} = \sum_{n=i-1}^{i+k-2} PRI[n]. \tag{7}$$

Performing the summation leads to

$$\begin{aligned} &d_{i,k} = k\cdot PRI_{max} - \frac{\Delta PRI}{2\cdot(N_{PRI}-1)}\cdot(2\cdot i + k - 3)\cdot k, \\ &\text{for } 1 \le i \le N_{PRI} + 1 - k; \\ &d_{i,k} = T_{cycle} - (N_{PRI} - k)\cdot PRI_{max} \\ &+\frac{\Delta PRI}{2\cdot(N_{PRI}-1)}\cdot(2\cdot i + k - N_{PRI} - 3)\cdot(N_{PRI} - k), \\ &\text{for } N_{PRI} + 2 - k \le i \le N_{PRI}. \end{aligned} \tag{8}$$

Note that, for a given $k = k_0$, the expressions $R_1[i] = c/2\cdot d_{i,k_0}$ and $R_2[i] = c/2\cdot\left(d_{i,k_0} + \tau_P\right)$ describe the boundaries of the k_0^{th} blockage region over the pulse index i. It can be shown that the minimum and maximum range of these regions are given by

$$\begin{aligned} &R^{block}{}_{min}(k_0) = \\ &\frac{c}{2}\cdot\left(k\cdot PRI_{max} - \frac{\Delta PRI}{2\cdot(N_{PRI}-1)}\cdot(N_{PRI} - k_0 - 1)\cdot k_0\right) \end{aligned} \tag{9}$$

$$R^{block}{}_{max}(k_0) = \frac{c}{2}\cdot\left(k\cdot PRI_{max} - \frac{\Delta PRI}{2\cdot(N_{PRI}-1)}\cdot(k_0-1)\cdot k_0 + \tau_P\right) \quad (10)$$

A meaningful criterion for the PRI variation is to ensure that the blockage regions do not overlap, i.e.

$$R^{block}{}_{min}(k+1) > R^{block}{}_{max}(k) \quad (11)$$

for all ks of interest within the swath. The violation of this condition would cause two large gaps at that range, impairing performance. Thus, it is required that

$$PRI_{max} - \frac{\Delta PRI}{N_{PRI}-1}\cdot\left((N_{PRI}-k)\cdot(k+1)+1\right) - \tau_P > 0. \quad (12)$$

However, provided that the sequence is long, $k\cdot N_{PRI} \gg 1$ and $N_{PRI}-k \cong N_{PRI}-1 \cong N_{PRI}$ and the condition can be simplified to

$$PRI_{max} - \Delta PRI\cdot(k+1) - \tau_P > 0. \quad (13)$$

Assuming that the maximum order of interest within the swath is $k_{max} = k+1$, the maximum PRI variation satisfying the criterion can be approximated as

$$\Delta PRI_{max} \cong \frac{PRI_{max}-\tau_P}{k_{max}}. \quad (14)$$

Following this criterion, the gap length for a given order k_0 becomes

$$T_{gap}(k_0) = T_{cycle}\cdot\frac{k_{max}}{k_0}\cdot\frac{\tau_P}{PRI_{max}-\tau_P}$$
$$T_{gap}(k_0) = T_{cycle}\cdot\frac{k_{max}}{k_0}\cdot\frac{\Delta_{cycle}}{1-\Delta_{cycle}}, \quad (15)$$

where Δ_{cycle} is the duty cycle and the substitution $\tau_P = \Delta_{cycle}\cdot PRI_{max}$ was used. A peculiarity of this mode is the dependency of the gap length on the duty cycle, which allows smaller gaps than in a typical ScanSAR, whose minimum is half of the cycle (for two sub-swaths). From (15), an equivalent gap of more than 50% is only obtained for $\Delta_{cycle} > 33\%$ – an unusually high value – meaning that as a rule shorter gaps are expected. This implies that the cycle time is used more efficiently, and moreover an increased control over the maximum squint is made possible, as Δ_{cycle} may be set arbitrarily.

This result also indicates a counter-intuitive "compression" of the gap duration for larger ranges (higher k_0). This is, however, convenient for SAR processing, since the Doppler rate decreases with increasing range [1] and thus a longer observation time T_{ill} is required to achieve the resolution requirement. To ensure its fulfillment for $k_0 = k_{max}$, the cycle time should satisfy

$$T_{cycle} = T_{ill} + T_{gap}(k_{max})$$
$$T_{cycle} = T_{ill}\cdot\frac{1-2\cdot\Delta_{cycle}}{1-\Delta_{cycle}}$$
$$T_{cycle} = \frac{\lambda\cdot R_{max}}{2\cdot v_p\cdot\delta_{AZ}}\cdot\frac{1-2\cdot\Delta_{cycle}}{1-\Delta_{cycle}}, \quad (16)$$

where λ, v_p and δ_{AZ} denote the wavelength, platform velocity and required azimuth resolution. The equation above gives a criterion for the design of the cycle time.

Figure 2 (a) shows an example blockage diagram for the system described in **Table 1**. The abscissa values show 3 cycles of duration $T_{cycle} = 3.58$ s. In this case, the swath is 400 km wide and the orders $17 < k < 24$ are relevant. For each of them, the regions highlighted in red represent the gaps

$$\frac{c}{2}\cdot d_{i,k} \le R_{gap}(k) \le \frac{c}{2}\cdot d_{i,k} + \tau_P, \quad (17)$$

whereas the light blue parallelogram represents the azimuth aperture, with an example beamwidth of 2.0°.

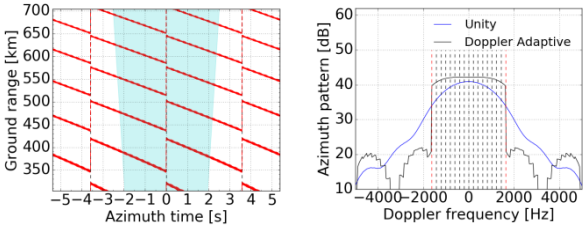

(a) (b)

Figure 2: Examples for parameters of **Table 1**. (a) Blockage diagram with all orders $17 \le k \le 24$ for a 400 km swath. (b) Azimuth patterns comparing unity beamforming and Doppler-adaptive beamforming (Section 2.2).

2.2 Azimuth Spectrum

In the case of the traditional ScanSAR mode, each subswath is imaged by a corresponding *burst* of pulses. For a given range, the time in which the system is illuminating the other swath(s) translates into a gap of duration T_{gap} over which no data are gathered, creating a (Doppler) spectral gap. The illumination time T_{ill} defines the acquired Doppler bandwidth of the signal, which should match the intended resolution. Its Doppler centroid is, however, determined by the target's position in azimuth with respect to the swath's illumination cycle, which repeats itself with period $T_{cycle} = T_{gap} + T_{ill}$.

Similarly, in the continuous PRI variation mode, the *burst* (here understood as a period of continuous illumination) is interleaved with (shorter) spectral gaps, as illustrated in **Figure 3**, in which the best and worst cases of Doppler centroid are highlighted. All targets within a particular range fall in between these two extreme cases. Even though the focusing uses only a single burst at a time (the one closest to a given zero Doppler time), it should be noted that each target is seen from at least one, but typically two, other bursts (cf. **Figure 3 (b)** and **(c)**), whose duration is potentially shorter than T_{ill}. This additional and free information could be used e.g. for interferometric *multilooking* or along-track velocity estimates exploring squint angle diversity.

2.3 Multichannel Beamforming Concept

To ensure adequate performance, the azimuth patterns should be made broad enough so that the signal has sufficient power even in the (high-squint) worst case. The lower gain may be compensated by the use of reflector architectures and beamforming. The rationale for the DBF concept presented in this section is that – since the total PRI variation ΔPRI is moderate and a very long

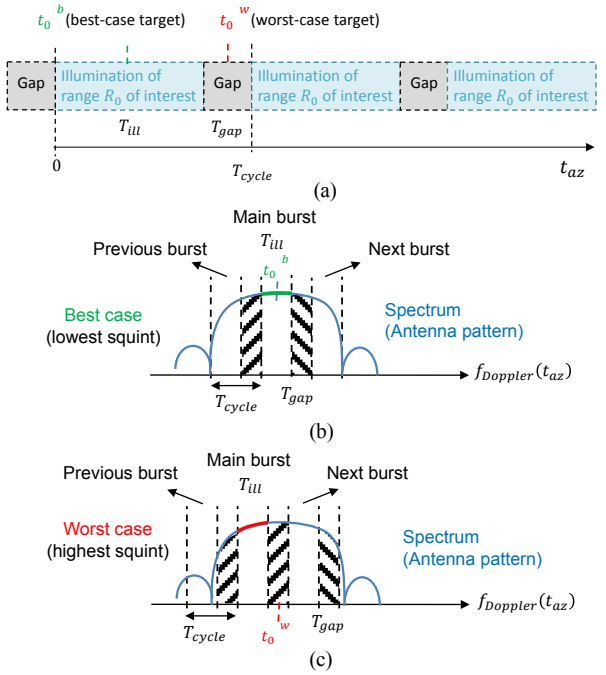

Figure 3: Schematic representation of spectral gaps. (a) Cycle time for a particular range, divided into the observation time T_{ill} and gap time T_{gap}. (b) Best case (no Doppler centroid): zero Doppler time t_0^b in the center of the illumination, the spectrum lies in the antenna's maximum gain region. (c) Worst case (highest Doppler centroid): zero Doppler time t_0^w in the center of the gap, causing data loss around the zero Doppler region.

sequence of PRIs is used ($N_{PRI} \gg 1$) – the PRIs can be assumed to be nearly constant over a short time window. For instance, for the parameters of **Table 1**, the PRI step between adjacent pulses is in the order of 0.7 ns. This means the azimuth sampling is locally regular, enabling the use of frequency-domain techniques for DBF, provided that the system possesses multiple digitized azimuth channels. For instance, a short-time FFT over azimuth with a small number of pulses (e.g. 8 or 16) could be used to efficiently implement the subdivision of the Doppler spectrum into an equivalent number of sub-bands, as illustrated in **Figure 4**. An alternative is a set of bandpass filters.

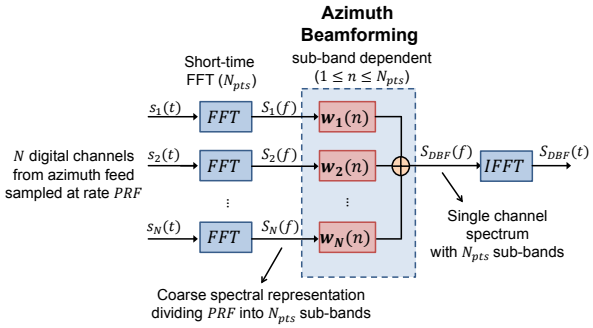

Figure 4: Block diagram for Doppler sub-band dependent azimuth DBF. The bands are separated using a short-time FFT (or equivalently a set of band-pass filters) and each sub-band undergoes DBF independently.

Each of the sub-bands receives different beamforming weights over azimuth. After combination over the azimuth channels and a short inverse FFT over the azimuth samples, a Doppler-dependent weighting is achieved. A matched-filter like beamformer (cf. [15],[16]) using the average of the patterns over the sub-bands is an interesting approach to maximize the gain. The pattern obtained in near range by applying this approach with $N_{pts} = 16$ (a FFT of this length [17] requires 68 real multiplications, as much as a 17-tap FIR filter, and 162 real additions) for the system of **Table 1** is shown in **Figure 2 (b)**, where it is compared to the unity beamformer (sum of the azimuth channels). Aliasing is taken into account, and the Doppler regions spaced by integer multiples of PRF receive the same weights. The improvement in the patterns is clear, both in terms of increased gain (2 to 5 dB) and sidelobe suppression. The latter is a consequence of the weight mismatch for the aliased bands, which produces a convenient "anti-aliasing" effect on the Doppler spectrum.

3 L-Band Design Examples

This section presents simulation results to assess the SAR performance of a multichannel reflector system in L-band. Section 3.1 illustrates the performance of the slowly varying PRI mode described in the previous sections, in the case of a 400 km swath imaged with 5 m azimuth resolution in single polarization. Section 3.2 describes the performance of a complementary multichannel staggered SAR mode [14],[18],[19], which could be applied to the same system to image the first 200 km of the swath with a finer 2.5 m resolution in quad-pol. The imaging requirements are azimuth ambiguity-to-signal ratio (AASR), range ambiguity-to-signal ratio (RASR) and noise equivalent sigma zero (NESZ) levels better than -25 dB.

3.1 Slowly Varying PRI mode

The system described in **Table 1** is based on a 12.0 m diameter reflector with a multichannel feed. The elements (30 in elevation and 6 in azimuth) are spaced at 0.6 λ, but they are summed pairwise in azimuth to yield 3 channels spaced at 1.2 λ. These are used to apply the method described in Section 2.3 with 16 sub-bands (cf. pattern in **Figure 2 (b)**). The PRI variation follows the considerations in Section 2.1.

The SAR performance is summarized in **Figure 5** in terms of the AASR, RASR, NESZ (cf. [20] for a discussion of this parameter's estimation from the patterns and system parameters) and azimuth resolution. The ambiguity level estimation for staggered SAR follows special considerations described in [17] in detail. For each parameter, the best and worst cases (cf. Section 2.2) are represented by green and red curves, respectively. The AASR and RASR are better than -37.3 dB and -26.9 dB. The very low azimuth ambiguity levels are a consequence of the high PRF and the very good sidelobe behavior of the azimuth patterns (cf. **Figure 2 (b)**).

Platform and swath parameters		Pulse and cycle parameters	
Orbit height h_{orbit}	773 km	Cycle time T_{cycle}	3.58 s
Swath width on ground	400 km	Gap duration	0.19 - 0.24 s
Incidence angle range	24.0 – 47.2 °	Worst-case illumination time	3.34 s
Reflector, feed and front-end parameters		PRF range	3.200 – 3.332 Hz
Diameter	12.0 m	Total PRI variation ΔPRI	12.4 µs
Focal length	12.0 m	Relevant orders (k_{min}, k_{max})	(17,24)
Feed offset in elevation	8.0 m	PRI sequence length N_{PRI}	11695
Center frequency	1.26 GHz	Pulse length τ_p	15.31 µs
Number of channels in elevation/azimuth	30 / 3	Duty cycle Δ_{cycle}	5%
Channel spacing in elevation/azimuth	0.8 λ / 1.2 λ	Average Tx power	475 W
Elevation tilt angle	31.8 °	Worst-case Doppler Centroid	726 Hz
Noise temperature	600 K	Chirp bandwidth	80 MHz
Feed loss	2 dB	Polarization	VV
DBF and processing parameters			
Total elevation beams	6	DBF sidelobe constraint	-36 dB
Active channels per SCORE beam	11	Processed bandwidth Bw_{proc}	1330 Hz

Table 1: Relevant system parameters for slowly varying PRI mode in L-band (single-pol).

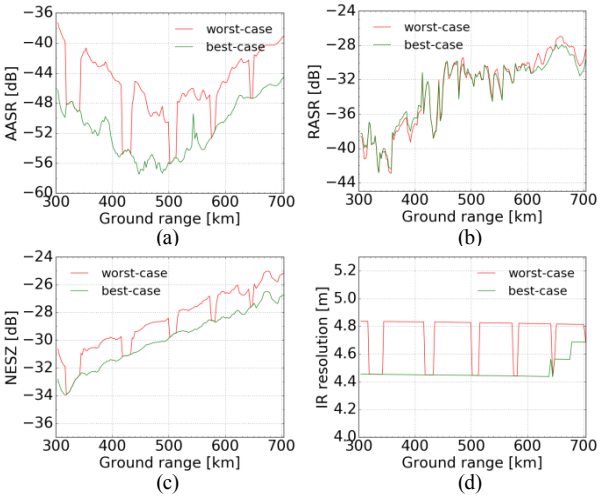

Figure 5: Simulated SAR performance of reflector system in slowly varying PRI mode. (a) AASR; (b) RASR; (c) NESZ and (d) azimuth resolution.

The RASR is kept low in spite of the high PRF by usage of the sidelobe-constrained beamformer described in [19] with a sidelobe level at least 36 dB below the peak level in the regions which yield range ambiguities for the whole PRF range. The RASR values are estimated for the mean PRF of 3266 Hz and the optimization is done for the worst-case (with squint), which degrades the best-case performance slightly but improves the worst-case performance, which is the driver in terms of fulfilling the requirements. The average power of 475 W is designed to yield an NESZ better than -25.0 dB in the worst case. The azimuth resolution is better than 4.84 m. The requirements of 5 m resolution and -25 dB ambiguity/NESZ are seen to be satisfied.

3.2 Multichannel staggered SAR mode

The system from **Table 1** possesses multiple azimuth channels and the capability of continuous PRI variation, and may also be employed for a multichannel staggered SAR mode using optimal mean square error resampling. The mode shows a reduced swath width but finer resolution. The parameters which differ from Section 3.1 are listed in **Table 2**, whereas the SAR performance is summarized in **Figure 6**.

Platform and swath parameters		Pulse parameters	
Orbit height h_{orbit}	773 km	Mean PRF $\overline{PRF}$	2 x 2650 Hz
Incidence angle range	24.0 – 37.0 °	Initial PRI PRI_0	204 µs
DBF and Processing parameters		PRI step Δ	-0.4 µs
Total elevation beams	4	PRI sequence length N_{PRI}	2 x 63
Active channels per SCORE beam	9	Pulse length τ_p	11.3 µs
DBF sidelobe constraint	-40 dB	Duty cycle Δ_{cycle}	6%
Processed bandwidth Bw_{proc}	3732 Hz	Average Tx power	310 W

Table 2: Relevant system parameters for multichannel staggered SAR mode in L-band (quad-pol).

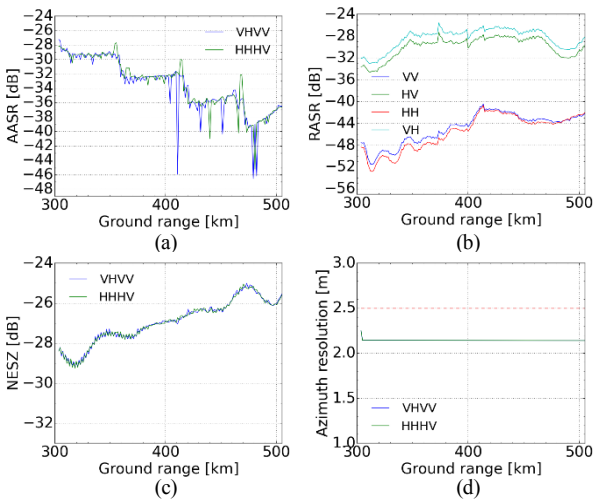

Figure 6: Simulated SAR performance of reflector system in multichannel quad-pol staggered SAR mode. (a) AASR; (b) RASR; (c) NESZ and (d) azimuth resolution.

The AASR and the NESZ (which is influenced by the beamformer's noise scaling) depend on the Tx polarization, which dictates different sampling instants [13]. The AASR is better than -27.2 dB, whereas the RASR is better than -25.6 dB. The average power of 310 W is adjusted to yield a NESZ better than -25.0 dB. The smaller average power is a consequence of the swath restriction to near range and the absence of squint for this mode. The azimuth resolution is better than 2.3 m, meaning all requirements are fulfilled.

4 Final Remarks

The paper analyzed and introduced a novel design criterion for a slowly varying PRI mode in which a slow, linear and cyclical variation is used to smoothly shift the gaps due to Tx events over the swath. The mode assumes multiple elevation beams and retains some properties of the ScanSAR mode (which may be portrayed as employing a particularly simple PRI variation scheme), but the illumination time is shown to be used more efficiently. The PRI variation scheme is simpler than the fast PRI variation of *staggered SAR* [13], also leading to simpler processing. The multiple elevation beam architecture requires multiple channels in elevation, however the overall antenna area is kept small. For instance, the required antenna aperture is reduced in the new mode by more than 35 % in comparison to the staggered SAR mode of Tandem-L, which will employ a reflector with a diameter of 15 m. Exploitation of the nearly constant PRF to implement a Doppler-frequency dependent azimuth beamforming is proposed to compensate for the lower gain. The mode offers also the opportunity to acquire additional looks with lower resolution that can be used for *multilooking* or observation of a target with angle of arrival diversity.

Simulations showed the possibility of imaging a 400 km swath in single or dual polarization at 5 m azimuth resolution with very good imaging performance in L-band. The same system could be employed in a multichannel fully polarimetric staggered SAR mode to yield a complementary coverage of the first half of the swath with 2.5 m resolution. Combined, the two modes allow the system to show excellent imaging performance.

References

[1] J. Curlander, R. McDonough: *Synthetic Aperture Radar: Systems and Signal Processing*, Jon Wiley & Sons, 1991.

[2] K. Tomiyasu: *Conceptual performance of a satellite borne wide swath synthetic aperture radar*, in IEEE Trans. Geosci. Remote Sens., vol. GRS-19, no. 2, pp. 108-116, April 1981.

[3] R. K. Moore, J. P. Claassen and Y. H. Lin: *A scanning spaceborne synthetic aperture radar with integrated radiometer*, in IEEE Trans. Aerosp. Electron. Syst., vol. AES-17, no. 3, pp. 410-421, May 1981.

[4] A. Currie, M. A. Brown: *Wide-swath SAR*, in IEE Proceedings F - Radar and Signal Processing, vol. 139, pp. 122-135, 1992.

[5] G. Callaghan, I. Longstaff: *Wide-swath spaceborne SAR using a quad-element array,* in IEE Proc. RSN, vol. 146, pp. 159-165, 1999.

[6] M. Suess, B. Grafmueller, R. Zahn: *A novel high resolution, wide swath SAR system*, in Proc. IGARSS, Sydney, Australia, 2001.

[7] G. Krieger, N. Gebert, and A. Moreira: *Multidimensional waveform encoding: A new digital beamforming technique for synthetic aperture radar remote sensing,* in IEEE Trans. Geosci. Remote Sens., vol. 46, no. 1, pp. 31–46, January 2008.

[8] G. Krieger, *et al.*: *Advanced Concepts for Ultra-Wide-Swath SAR Imaging*, in 7th European Conference on Synthetic Aperture Radar (EUSAR 2008), pp. 1-4, Friedrichshafen, Germany, 2008.

[9] G. Krieger *et al.*: *SIMO and MIMO System Architectures and Modes for High-Resolution Ultra-Wide-Swath SAR Imaging*, in 11th European Conference of Synthetic Aperture Radar (EUSAR*)*, pp. 1-6., Hamburg, 2016.

[10] M. Younis *et al.*, *Techniques and Modes for Multi-Channel SAR Instruments*, in 11th European Conference of Synthetic Aperture Radar (EUSAR), pp. 1-6., Hamburg, 2016.

[11] M. Suess and W. Wiesbeck: Side-looking synthetic aperture radar system, European Patent EP 1 241487, Sept., 2002.

[12] N. Gebert, G. Krieger and A. Moreira: *Digital Beamforming on Receive: Techniques and Optimization Strategies for High-Resolution Wide-Swath SAR Imaging*, in IEEE Trans. Aerosp. Electron. Syst., vol. 45, no. 2, pp. 564-592, 2009.

[13] M. Villano, G. Krieger and A. Moreira: *Staggered SAR: High-Resolution Wide-Swath Imaging by Continuous PRI Variation*, in IEEE Trans. Geosci. Remote Sens., vol. 52, no.7, pp.4462-4479, 2014.

[14] F. Queiroz de Almeida and G. Krieger: *Multichannel Staggered SAR Azimuth Sample Regularization*, in 11th European Conference on Synthetic Aperture Radar (EUSAR 2016), pp. 1-6, Hamburg, Germany, 2016.

[15] H. L. V. Trees: *Optimum Array Processing*, New York: John Wiley & Sons Inc., 2002.

[16] S. Huber, A. Patyuchenko, G. Krieger and A. Moreira: *Spaceborne Reflector SAR Systems with Digital Beamforming*, in IEEE Trans. Aerosp. Electron. Syst., vol. 48, no. 4, pp.3473-3493, 2012.

[17] B. Porat, *A Course in Digital Signal Processing*, New York: John Wiley & Sons Inc., 1997.

[18] M. Villano, G. Krieger and A. Moreira: *Ambiguities and image quality in staggered SAR,* in 5th Asia-Pacific Conference on Synthetic Aperture Radar (APSAR), pp. 204-209, Singapore, 2015.

[19] F. Queiroz de Almeida, M. Younis, G. Krieger and A. Moreira: *Multichannel Staggered SAR Azimuth Processing,* IEEE Transactions on Geoscience and Remote Sensing, vol. 56, no. 8, 2018.

[20] F. Queiroz de Almeida, T. Rommel, M. Younis, G. Krieger and A. Moreira: *Multichannel Staggered SAR: System Concepts with Reflector and Planar Antennas,* in revision IEEE Transactions on Aerospace and Electronic Systems, 2017.

[21] M. Younis, P. López-Dekker and G. Krieger: *Signal and noise considerations in multi-channel SAR*, in 2015 16th International Radar Symposium (IRS), Dresden, pp. 434-439., 2015.